ADVANCED MATERIALS
www.advmat.de

Size-Dependent Multiexciton Dynamics Governs Scintillation From Perovskite Quantum Dots

Andrea Fratelli, Matteo L. Zaffalon, Emanuele Mazzola, Dmitry N. Dirin, Ihor Cherniukh, Clara Otero-Martínez, Matteo Salomoni, Francesco Carulli, Francesca Rossi, Francesco Meinardi, Luca Gironi, Liberato Manna, Maksym V. Kovalenko,* and Sergio Brovelli**

The recent emergence of quantum-confined nanomaterials in the field of radiation detection, in particular lead halide perovskite nanocrystals, offers scalability and performance advantages over conventional materials. This development raises fundamental questions about the mechanism of scintillation itself at the nanoscale and the role of particle size, arguably the most defining parameter of quantum dots. Understanding this is crucial for the design and optimization of future nanotechnology scintillators. In this work, these open questions are addressed by theoretically and experimentally studying the size-dependent scintillation of $CsPbBr_3$ nanocrystals using a combination of Monte Carlo simulations, spectroscopic, and radiometric techniques. The results show that the simultaneous effects of size-dependent energy deposition, (multi-)exciton population, and light emission under ionizing excitation, typical of confined particles, combine to maximize the scintillation efficiency and time performance of larger nanocrystals due to greater stopping power and reduced Auger decay. The agreement between theory and experiment produces a fully validated descriptive model that predicts the scintillation yield and kinetics of nanocrystals without free parameters, providing fundamental guidance for the rational design of nanoscale scintillators.

1. Introduction

Ionizing radiation detection is critical across diverse domains such as precision medicine,[1,2] industrial[3] and national security,[4] environmental monitoring,[5] energy management,[5] and cutting-edge scientific research in high-energy physics[6] (HEP) at particle accelerators in the search for rare events in nuclear physics. In these applications, scintillator materials play a crucial role by converting ionizing radiation into detectable signals using high-performance photosensors such as phototubes or silicon photomultipliers (SiPMs). Ideal scintillators should feature compositions rich in high atomic number (Z) elements, ensuring a high probability of interaction with radiation (proportional to Z^n, $n = 1$–5 depending on the radiation type and interaction process),[7,8] along with high density, stability to radiation (so-called radiation hardness), efficiency, and speed of emission processes, which is

A. Fratelli, M. L. Zaffalon, F. Carulli, F. Meinardi, S. Brovelli
Dipartimento di Scienza dei Materiali
Università degli Studi di Milano-Bicocca
Via R. Cozzi 55, Milano 20125, Italy
E-mail: sergio.brovelli@unimib.it

E. Mazzola, M. Salomoni, L. Gironi
Dipartimento di Fisica
Università degli Studi di Milano-Bicocca
Piazza della Scienza 3, Milano 20126, Italy

E. Mazzola, L. Gironi, S. Brovelli
INFN–Sezione di Milano–Bicocca
Milano 20126, Italy

D. N. Dirin, I. Cherniukh, M. V. Kovalenko
Department of Chemistry and Applied Biosciences
ETH Zürich
Zürich 8093, Switzerland
E-mail: mvkovalenko@ethz.ch

D. N. Dirin, I. Cherniukh, M. V. Kovalenko
Laboratory for Thin Films and Photovoltaics and Laboratory for Transport at Nanoscale Interfaces
Empa–Swiss Federal Laboratories for Materials Science and Technology
Dübendorf 8600, Switzerland

C. Otero-Martínez, L. Manna
Nanochemistry
Istituto Italiano di Tecnologia
Via Morego 30, Genova 16163, Italy
E-mail: liberato.manna@iit.it

M. Salomoni
European Organization for Nuclear Research (CERN)
Esplanade des Particules 1
Meyrin 1211, Switzerland

F. Rossi
IMEM-CNR Institute
Parco Area delle Scienze 37/A, Parma 43124, Italy

The ORCID identification number(s) for the author(s) of this article can be found under https://doi.org/10.1002/adma.202413182

DOI: 10.1002/adma.202413182

especially vital in Time-of-Flight-based technologies like positron emission tomography[9] (ToF-PET) and high-brightness beam detection.[10,11]

The figure of merit for ToF-PET is the coincidence time resolution,[12] $CTR = 3.33\sqrt{(\tau_{RISE} \times \tau_{EFF})/\Gamma}$, where τ_{RISE} is the signal risetime (typically due to the detection chain) and $\tau_{EFF} = (\sum_i \frac{R_i}{\tau_i})^{-1}$ is the effective scintillation lifetime[11] (rate $k_{EFF} = \frac{1}{\tau_{EFF}}$) obtained, in case of multi-exponential decay kinetics, as the harmonic average of the i-th scintillation decay components weighted by their respective time-integrated relative contributions R_i. The term $\Gamma = \Phi_{SCINT} \times E \times \beta \times \chi$ is the intensity of the scintillation signal that depends on the scintillation efficiency (Φ_{SCINT}), on the amount of energy (E) deposited in the scintillator, on the light outcoupling efficiency (β), and on the quantum efficiency of the coupled photodetector (χ). The quantity $LY = \Phi_{SCINT} \times E \times \beta$ is commonly referred to as the light yield and corresponds to the number of emitted photons per unit of energy deposited.[7] In the ToF-PET field, the main challenge is to achieve CTR≤10 ps that would significantly reduce the acquisition time (most accurate commercial devices feature CTR values ≈200 ps) while improving the signal-to-noise ratio,[2,10] leading to millimeter spatial resolution in cancer diagnostics and providing high image quality at reduced doses. In the case of HEP experiments, the push to explore the limits of the Standard Model at the frontiers of energy and intensity requires experiments to operate at ever-higher rates.[5] Scintillation detectors for the High-Luminosity Large Hadron Collider (HL-LHC) and Future Circular Collider (FCC) era will require time resolutions on the order of a few tens of ps or less, with double-pulse separation at the level of a few ns. In this case, there is no exhaustive figure of merit regarding the timing performance as with CTR but, similarly to ToF-PET, the timing resolution is given by the variance with which enough photoelectrons are collected to provide a statistically relevant signal (hence often quantified in terms of photons MeV^{-1} ns^{-1}).

In both fields, the main obstacle to achieving the required energy and temporal resolution lies in the limitations of scintillator materials that are often chosen based on a trade-off between their performance, cost, and availability. Inorganic crystals[13] offer high efficiency and energy resolution but are slow, expensive, and difficult to mass-produce, whereas plastic scintillators[14] are cost-effective and fast emitting but suffer from low density, efficiency, and radiation hardness. To address the drawbacks of both types and capitalize on their strengths, nanocomposite scintillators have emerged recently.[15,16] These scintillators feature optical-grade plastic matrices as the waveguiding component, while high-Z nanocrystals (NCs) synthesized using scalable chemical techniques provide scintillation.[15,17,18] Importantly, using NCs as nano scintillators in host matrices not only offers a solution to overcome the scalability limitations of conventional materials but also an avenue to enhance the scintillation performance. This is due to the unique photophysics of quantum-confined materials, providing size-tunable emission spectra that match perfectly with the spectral sensitivity of light detectors and ultrafast sub-nanosecond scintillation kinetics resulting from the recombination of multiexciton generated upon interaction with ionizing radiation, as demonstrated recently across various classes of NCs.[16,18–20]

One category of nanomaterials that has garnered particular attention within this context is lead halide perovskite NCs (LHP-NCs),[21–24] with $CsPbBr_3$ emerging as the dominant player.[21,25,26] These materials feature a composition based on heavy metals, remarkable resistance to radiation,[18,23,27] extensive scalability facilitated by low-temperature methods,[28,29] and efficient, fast scintillation[19,24,30] owing to the unique tolerance to structural defects.[31] In recent years, there has been a growing body of research aimed at optimizing their scintillation and developing nanocomposites for various radiation detection applications,[32] particularly X-ray detectors and screens utilized in medical imaging and object inspection. Time-resolved scintillation studies have further demonstrated ultrafast radioluminescence kinetics due to substantial contributions by the recombination of biexcitons (indicated as *XX*; *X* denotes single exciton species) generated upon interaction with ionizing radiation, which is particularly promising for fast-timing applications.[18,19]

To fully exploit the potential of nanoscale materials for radiation detection, it is essential to fully understand and control the key parameters that govern the scintillation processes, which, as we demonstrate below, are strongly size-dependent. For example, particle size has a strong influence on the amount of energy deposited within a single NC after ionizing excitation, resulting in size-dependent exciton occupancy. The resulting multiexciton scintillation is also affected by nonradiative Auger recombination (AR)—that is the nonradiative annihilation of one exciton in favor of a third carrier[33]—whose rate increases with the inverse of the particle volume ($k_{AR} \propto V^{-1}$).[34] Overall, this leads to an interplay between size effects on the scintillation yield and time kinetics, which requires a detailed understanding for proper material optimization.

Here we aim to fill this gap by studying the effect of particle size on the scintillation efficiency and kinetics of $CsPbBr_3$ NCs ranging from $d = 3$ nm (lateral size) to $d = 15$ nm, with tunable emission from 470 to 520 nm. The dependence of scintillation intensity of single NCs (I^{NC}_{SCINT}) and NC ensembles (I^{ENS}_{SCINT}) and τ_{EFF} on particle size is first theoretically analyzed through the combination of the emission rate equations in the multiexciton regime and Geant4 Monte Carlo simulations,[35] and then experimentally validated, yielding an intertwined parameter space where the size-dependent initial exciton population per NC (denoted as $\langle N \rangle$), the AR rate and the fluorescence efficiency are the key elements. We have experimentally evaluated all the key parameters necessary to describe the scintillation mechanisms using a combination of optical spectroscopies and radiometric experiments as summarized in **Scheme 1a**. X-ray attenuation and scintillation experiments, confirmed by Monte Carlo simulations, showed that the stopping power of NC ensembles with the same total mass is independent of particle size, while the energy deposition within a single NC increases with size, closely resembling the carrier multiplication phenomenology. This leads to substantially higher $\langle N \rangle$-values for larger particles making high-order exciton contributions gradually more relevant, as confirmed by time-resolved radioluminescence (RL) experiments. Consistent with the literature,[36–38] AR was found to be efficient in all NC samples, resulting in scintillation dominated by single-exciton photoluminescence (PL) efficiency (Φ_X) and progressive acceleration of τ_{EFF} with increasing NC size due to reduced AR quenching of the ultrafast *XX* decay. The whole body of experimental data

a

	Method	Quantity of interest
Theoretical model for single NCs	Rate equations	Scintillation intensity (I^{NC}_{SCINT}) and kinetics (τ_{EFF})
	Geant4 Simulation	Energy deposited in NCs ($\langle N \rangle$ vs d)
Experimental validation on NC ensembles	X-rays absorption	Stopping power vs. d
	Photoluminescence, Transient absorption	ϕ_X , ϕ_{XX} , ϕ_{AR} τ_X , τ_{XX} , τ_{AR}
	Radioluminescence (cw, time resolved)	Scintillation intensity (I^{ens}_{SCINT}), $\langle N \rangle$ vs d, τ^{exp}_{EFF}
Validated model for NC-based scintillators		I^{ens}_{SCINT}, τ^{ens}_{EFF}

b

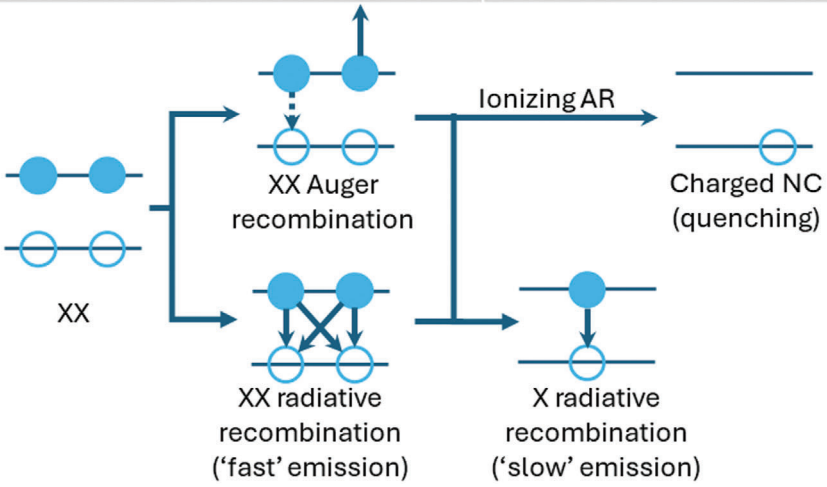

Scheme 1. a) Theoretical and experimental approaches for a validated model for the scintillation of NCs. b) Schematic depiction of the possible decay channels for biexcitons created upon ionizing excitation.

validates, with no free parameters, the theoretical model, which disentangles the single-particle and ensemble effects on the size dependence of NCs scintillation and provides guidelines for tailored technological optimization of nanoscale materials in radiation detection.

2. Results and Discussion

To accurately describe size effects on NC-based scintillators, it is necessary to consider both single-particle and ensemble effects. Single-particle effects concern the response of individual NCs to ionizing radiation, such as interaction property, stopping power, and AR-dependent emission efficiency. Ensemble effects, on the other hand, are crucial for the engineering of NCs-based scintillator detectors. Consider, for example, that for the same mass of scintillator material (M), a nanocomposite scintillator contains an amount of NCs (n_{NC}) that is proportional to the inverse of their volume ($n_{NC} = M/\rho V_{NC}$, where ρ is the density), which can introduce a large scaling factor for single-particle characteristics (e.g., $n_{NC}(d = 3\ \text{nm})/n_{NC}(d = 10\ \text{nm}) \sim 30$). We therefore begin with the single-NC treatment, which will then be implemented with ensemble considerations to provide us with a realistic interpretative model of the experimental findings. As the purpose of this work is to provide guidelines for NC selection and design, we focus on isolated noninteracting particles and leave the extension of our treatment to dense NC solids to a dedicated study.

Theoretical considerations on the impact of the NC size on the scintillation parameters. A discussion of the role of size in the scintillation of NCs requires addressing fundamental aspects of the NC photophysics under ionizing excitation that determines high-order exciton populations subject to AR. For the sake of this discussion, we do not consider nonradiative decay pathways other than AR (e.g., trapping, multi-phonon relaxation, that is, we consider an X emission efficiency of $\Phi_X = 1$) and neglect the case of trions as they have been experimentally shown to give a relatively minor contribution to the scintillation kinetics[19] and whose formation is situational as it largely depends on trapping processes. In the absence of AR, XX radiatively decays into an X species via the emission of a photon with an accelerated radiative rate due to increased emission statistics ($k_{XX} = 4k_X$ where k_X is the X radiative rate[33]), giving rise to a bi-exponential scintillation decay profile consisting of a fast XX component followed by a slower

one due to the resulting *X* (see Scheme 1b).[18,19,29,39] Auger decay involves the annihilation of a first exciton and the simultaneous promotion of a second carrier (belonging to the second exciton) to an energy equal to twice the energy gap. If this additional energy exceeds the ionization energy of the material, AR ionizes the NC and quenches the emission completely.[40] Alternatively, in the nonionising AR case, the hot carrier rapidly thermalizes back to the band edge, constituting a secondary *X*. In the absence of other nonradiative processes, such as trapping of hot carriers, as it occurs in B-type blinking,[41] this results in a net loss of half the photons that would be emitted if both excitons recombined radiatively. This is relevant for addressing the scintillation kinetics because the acceleration of the *XX* contribution is accompanied by the repopulation of *X* species that modify τ_{EFF} and partially compensate the light loss. The interplay between these recombination mechanisms of individual NCs in the *XX* regime is better understood considering the characteristic rate equations under instantaneous excitation (we hereby describe all processes through their rate for clarity),

$$\dot{N}_X = -N_X^0 k_X + N_{XX}^0 \left(k_{XX} + k_{AR}\xi\right) \quad (1)$$

$$\dot{N}_{XX} = -N_{XX}^0 \left(k_{XX} + k_{AR}\right) \quad (2)$$

where N_X^0 and N_{XX}^0 are the initial *X* and *XX* Poissonian populations following primary ionizing excitation obtained as:

$$N_X^0 = \langle N\rangle^2 \, e^{-\langle N\rangle} \quad (3)$$

$$N_{XX}^0 = \langle N\rangle \times \left(1 - \langle N\rangle \, e^{-\langle N\rangle} - e^{-\langle N\rangle}\right) \quad (4)$$

The population of *X* generated indirectly by the decay of *XX* via a radiative pathway or following AR is accounted for by the positive term in Equation (1). The probability of undergoing ionization following AR is expressed by the term $(1-\xi)$. The solutions to Equations (1) and (2) are, respectively,

$$N_X(t) = \left[N_X^0 + N_{XX}^0 \frac{k_{AR}\xi + k_{XX}}{k_{XX} + k_{AR} - k_X}\left(1 - e^{-\left(k_{XX}+k_{AR}-k_X\right)t}\right)\right] e^{-k_X t} \quad (5)$$

$$N_{XX}(t) = N_{XX}^0 \, e^{-\left(k_{XX}+k_{AR}\right)t} \quad (6)$$

Solving Equations (1) and (2) in the steady state gives the analytic expression of I_{SCINT}^{NC} emitted by a single NC particle following the creation of $\langle N\rangle$ excitons by an ionising photon:

$$\mathrm{I}_{\mathrm{SCINT}}^{\mathrm{NC}}(\langle N\rangle) \propto \Phi_X \left(N_X^0 + N_{XX}^0 \Phi_{XX} + N_{XX}^0 \Phi_{AR}\xi\right) + N_{XX}^0 \Phi_{XX} \quad (7)$$

where the *X* and *XX* processes contribute through their respective Φ_X, $\Phi_{XX} = 4k_X/(4k_X + k_{AR})$ and relative populations, which in turn depend on $\Phi_{AR} = k_{AR}/(4k_X + k_{AR})$. Essentially, Equation (7) allows for disentangling the *X* and *XX* contributions to the scintillation of single NCs which depend on the NC size through the corresponding Φ_{AR} and $\langle N\rangle$. Similarly, Equations (5) and (6) describe the time kinetics of the scintillation process and allow the determination of τ_{EFF} in a similar way to the experimental data. Together with Equation (7), this enables predicting the single particle timing performance through the quantity, $CTR_{NC} \propto \sqrt{\frac{\tau_{EFF}}{I_{SCINT}}}$. We underline that Equations (1–7) are valid for any excitation source and thus hold also for any optoelectronic/photonic application involving the recombination of biexcitons.

The simulated τ_{EFF}, I_{SCINT}^{NC}, and CTR_{NC} values computed using $k_X = 10^{-4}\ ps^{-1}$ (corresponding to an *X* lifetime of 10 ns typical of most UV–Vis emitting NCs), $\Phi_{AR} = 0 - 0.99$ and $\xi = 0.5$ are shown in **Figure 1a** (see Figure S1, Supporting Information for the simulations with $\xi = 0$ and 1), where we have treated all excitons with order higher than one as *XX*. Increasing $\langle N\rangle$ from 0.3 to 3.3, which is associated with situations in which larger amounts of energy are deposited within a NC, results in the gradual enhancement of I_{SCINT}^{NC}. On the other hand, efficient AR reduces I_{SCINT}^{NC} by quenching higher-order excitons.

The evolution of τ_{EFF} is more complex. On the one hand, it gradually accelerates with increasing $\langle N\rangle$ due to the increasing *XX* contributions, and on the other hand, it follows a nonmonotonic trend with the AR efficiency, which initially accelerates τ_{EFF} by speeding up the *XX* decay, but as it approaches unity completely suppresses the *XX* contribution, resulting in a much slower kinetics, essentially determined solely by the *X* decay. As a result, CTR_{NC} improves (accelerates) substantially with $\langle N\rangle$ and is only weakly worsened by AR. In fact, the crucial aspect that emerges from this analysis is the importance of $\langle N\rangle$ generated as a result of ionizing interaction in both light output and timing, pointing to the technological relevance of maximizing the single particle energy retention, while NC engineering for suppressing AR is relevant for maximizing the scintillation intensity but plays a relatively minor role in the timing performance.

Therefore, to investigate the role of size on the energy retention capability of NCs (responsible for $\langle N\rangle$), we computed the fraction of energy deposited within single NCs of increasing size (from $d = 2$ to 15 nm) following a photoelectric event producing electrons with energy $E = 1$–100 keV (schematic representation of a representative case with E = 7 keV is shown in Figure 1b). The Geant4 simulation[35] shows that for any initial energy, in the investigated size range, the energy deposited within a single NC grows with *d* (Figure 1c), with the smallest NCs releasing almost all of the initial electron energy into the outer medium. In the case of $E = 7$ keV (corresponding to the average energy of the X-rays used in our experiments), the energy deposited ranges from 5 to 35 eV for the smallest and the largest $CsPbBr_3$ NCs, corresponding to 2–13 times the corresponding energy gap (E_g). This trend highlights the instructive analogy between the excitation phase of the scintillation process (which gives rise to $\langle N\rangle$) and carrier multiplication,[43] a process that has been studied in detail in NCs,[44] where the number of band edge excitons produced scales linearly with the absorbed energy divided by the absorber E_g, and the angular coefficient is the inverse of the electron-hole pair formation energy ($\varepsilon_{e\text{-}h}$, in bulk semiconductors $\varepsilon_{e\text{-}h} \sim 2.8E_g$).[42] The inset of Figure 1c shows the expected trend for an example case where $\varepsilon_{e\text{-}h}$ is fixed at the bulk limit, motivated by the fact that the NCs states populated under high energy radiation are not subject to quantum confinement. As demonstrated below, this predicted $\langle N\rangle$-trend agrees remarkably well with the experimental results, enabling us to match the experimental τ_{EFF}, I_{SCINT}^{NC}, and CTR_{NC}-values with the respective curves in Figure 1a (highlighted as coloured dots).

Spectroscopic and scintillation experiments on $CsPbBr_3$ NCs of increasing size. To experimentally validate the theoretical framework just presented we performed optical spectroscopy and RL

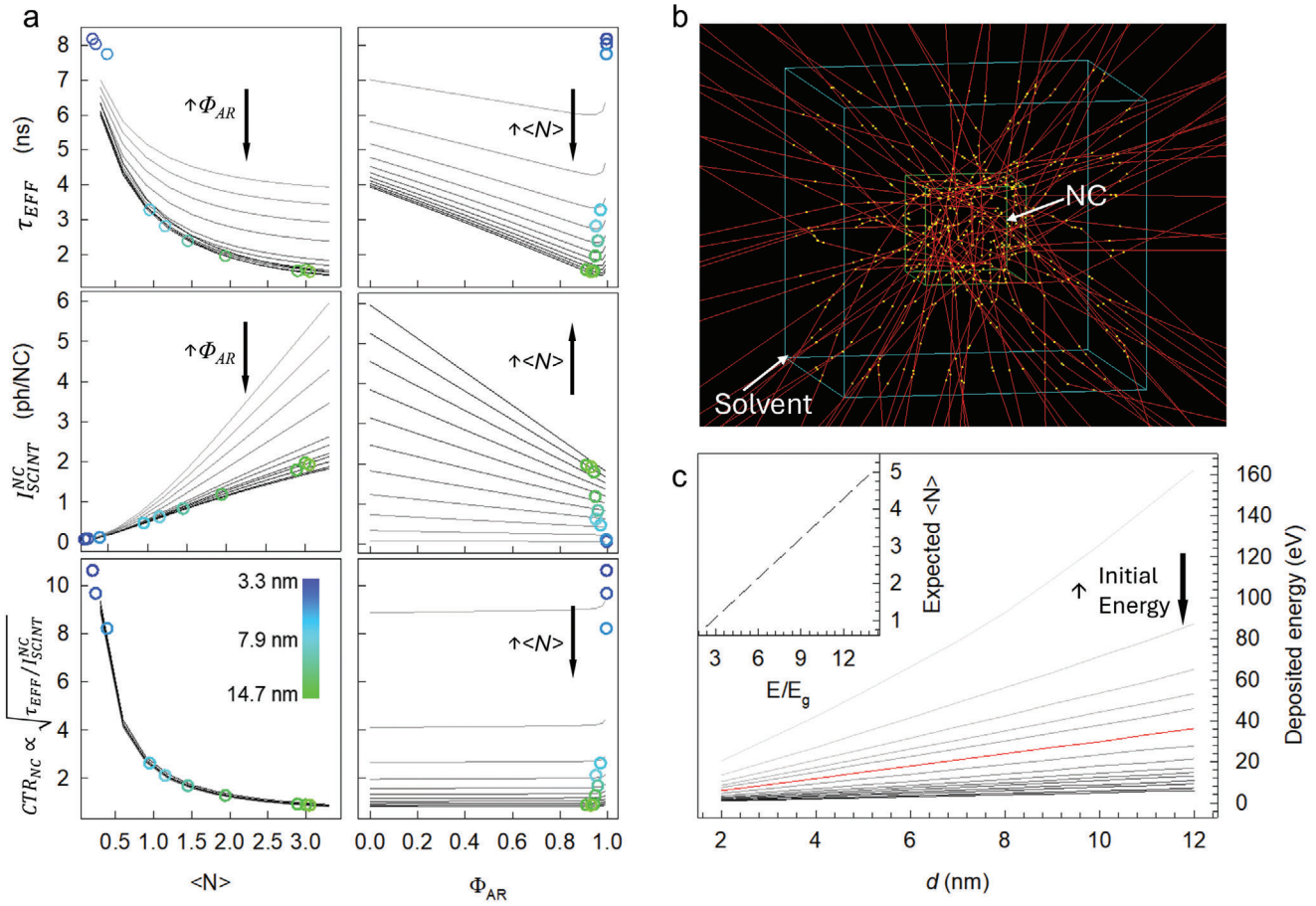

Figure 1. a) Simulation of the effective lifetime (τ_{EFF}), the single-particle scintillation intensity (I^{NC}_{SCINT}), and the square root of their ratio ($\propto CTR_{NC}$) as a function of the particle size for increasing values of $\langle N \rangle$ (0.3–3.3) or Φ_{AR} (0–0.99). Arrows indicate increasing Φ_{AR} or $\langle N \rangle$. Colored circles represent the experimental values obtained for $CsPbBr_3$ NCs with increasing size from 3.3 to 14.7 nm (from blue to green, legend in the bottom panel) b) Schematic representation of the simulation using Geant4 of the energy release inside a single NC following a photoelectric event with E = 7 keV. c) Results of the simulation of deposited energy with respect to the NC size, the red line corresponds to E = 7 keV) The black arrow indicates increasing initial electron energy (E = 1–100 keV). Inset: simulation of the expected $\langle N \rangle$ with respect to the deposited energy (expressed as number of bandgaps) computed considering the bulk electron-hole pair formation energy $\varepsilon_{e\text{-}h} \approx 2.8 E_g$.[42]

experiments on $CsPbBr_3$ NCs of increasing size from ≈3 to ≈15 nm. The particles were of cubic shape and orthorhombic crystalline phase, as shown in the high-resolution transmission electron microscope images of representative samples in **Figure 2a** and respective X-ray diffraction patterns (Figures S2 and S3, Supporting Information). The corresponding optical absorption and PL spectra are reported in Figure 2b, showing the progressive blue shift for decreasing NC sizes due to increasing quantum confinement.[45] The PL yield (measured at low excitation fluence to ensure an *X* photophysics, Figure 2c) spanned non-monotonically from $\Phi_X = 12\%$ to 80%, with the smallest and largest particles systematically showing lower efficiency, consistent with common observation of better surface passivation for intermediate sized NCs (i.e., 7 nm $\lesssim$ d $\lesssim$ 11 nm). The respective PL dynamics (Figure S4, Supporting Information) showed single exciton effective lifetimes ≈10 ns in all cases, with a measurable lengthening for the largest NCs consistent with the stronger symmetry forbidden *s-p* character of the radiative transition in large particles.[46] We next investigated the photophysics versus size in the multi-excitonic regime by performing TA measurements as a function of increasing excitation fluence.[36–38] The 1S bleach dynamics are shown in Figure 2d for representative NC samples with d = 10.7 nm and 3.3 nm (the whole set of data is reported in Figure S5, Supporting Information). At low excitation fluence (i.e., the *X* regime), all samples showed the characteristic peak at their respective band-edge energy due to bleaching of the 1S exciton absorption at all times[36] (Figure S6, Supporting Information). The corresponding time dynamics were essentially single exponential (except for a minor fast portion due to residual charge trapping) with characteristic time, τ_X~8 ns, matching the corresponding PL kinetics. Upon increasing the excitation fluence, a low energy shoulder appeared in the TA spectra, consistent with the attractive character of *XX* in $CsPbBr_3$ NCs[36,38] and the TA dynamics developed an initial ultrafast component due to *XX* decay with amplitude following the Poisson biexciton state-filling statistics[47] ($\approx \langle N \rangle^2$, Figure S7, Supporting Information). Higher excitation fluences gave rise to a high-energy shoulder with even more accelerated decay due

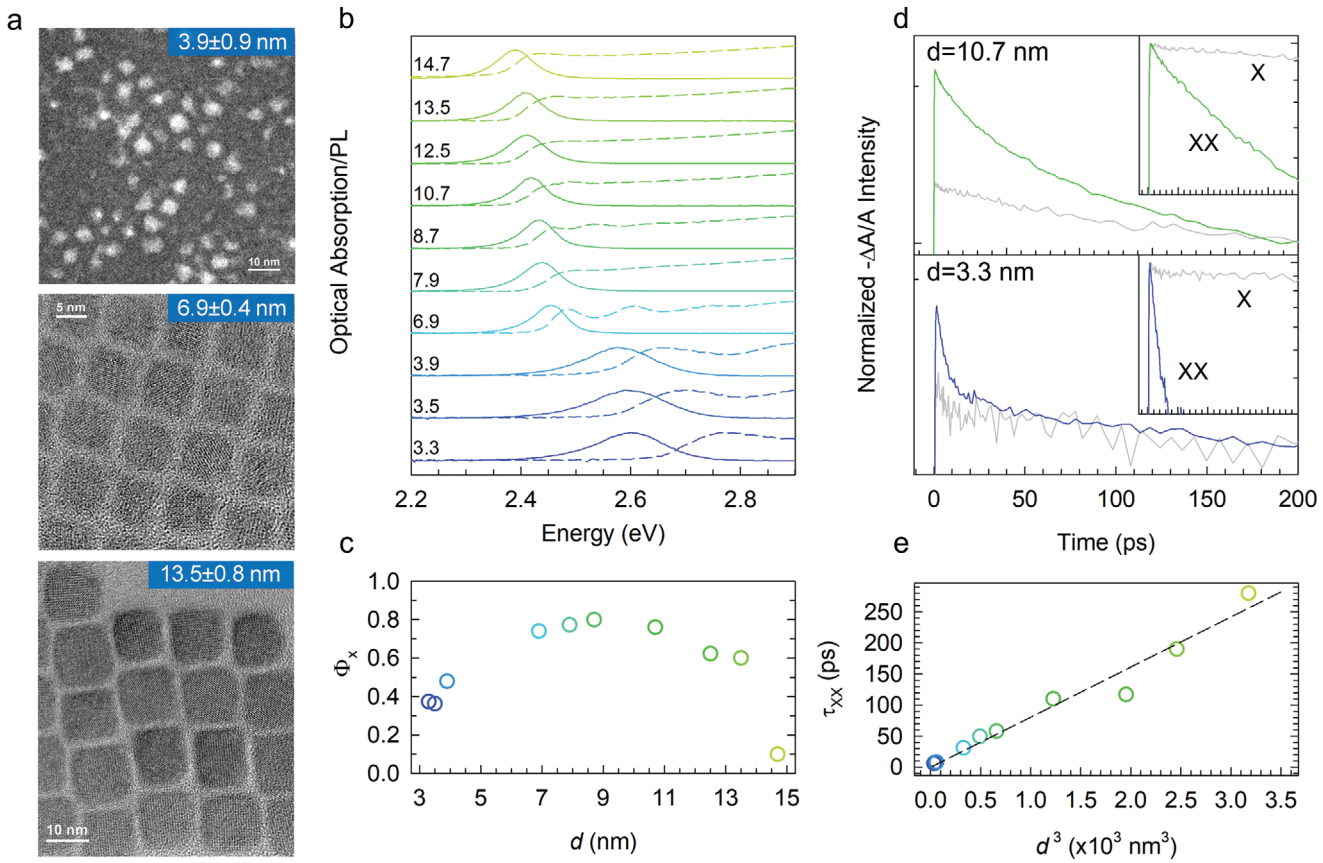

Figure 2. a) STEM-HAADF (d = 3.9 nm) and HRTEM (d = 6.9 nm, d = 13.5 nm) images for a representative set of $CsPbBr_3$ NCs. b) Normalized optical absorption (dashed lines) and PL spectra (solid lines) of the complete sample set (respective NC size in nm is indicated). c) PL quantum efficiency values measured in single exciton regime with respect to the NC size. d) TA dynamics for 10.7 and 3.3 nm NC for $\langle N \rangle = 0.16$ (grey lines) and $\langle N \rangle = 1.8$ (green, blue line) at their respective 1S bleach maximum. Inset: single exciton and biexciton components (time axis 0–100 ps with major ticks every 20 ps) extracted by the successive subtraction method.[33] e) Biexciton lifetimes, τ_{XX}, as a function of the NC volume. Dashed line, best linear fit highlighting the volume scaling.

to higher-order multiexcitons. To extract the *XX* and AR rates (k_{XX}, k_{AR}) and corresponding efficiencies (Φ_{XX},Φ_{AR}), we normalized the TA dynamics to their slow *X* tail and progressively subtracted curves with increasing $\langle N \rangle$.[36,38] The obtained *XX* decay curves are shown in the inset of Figure 2d (and in Figure S8, Supporting Information). The *XX* lifetimes of the whole sample set are shown in Figure 2e following the universal volume scaling law.[36,37] The corresponding Φ_{AR}-values spanned from ≈90% for the largest particles to ≈99% for strongly confined NCs, in good agreement with the literature.[36,37,48]

We then proceeded to study the scintillation behavior in order to experimentally measure the actual exciton occupancy $\langle N \rangle$created upon ionizing X-ray excitation and the RL intensity/timing versus *d*. As a first step, we verified that the X-ray attenuation of NC solutions with a given $CsPbBr_3$ mass content is size-independent, as this is closely related to the RL excitation rate. To this end, we measured the RL of a $Bi_4Ge_3O_{12}$ (BGO) crystal with and without interposed NC solutions ($d = 3.9$ vs 10.7 nm) with identical band-edge absorption between the scintillator and the X-ray source. The ratio between the acquired RL intensities with and without samples partially blocking the X-ray beam estimated the fraction of transmitted X-rays. In parallel, we used Geant4 simulations to calculate the energy deposited in two samples containing identical amounts of $CsPbBr_3$, one in the form of a single NC with $d = 12.6$ nm and the other in the form of 74 NCs with $d = 3$ (both having a total volume of 2000 nm^3). The calculations were also performed for different NC concentrations by simulating varying matrix sizes from 0.125 to 27 μm^3. As shown in **Figure 3a**, both the calculations and the experiment confirmed that the total stopping power was independent of the NC size, consistent with the fact that the samples had identical average densities. This enables us to quantitatively compare the RL intensity of NC solution with the same mass concentration. For all investigated samples, the RL spectra shown in Figure 3b matched the corresponding PL (the PL peak positions are marked with a tick on top of the corresponding RL curve), indicating that light emission was due to pure excitonic recombination with negligible influence from defect states under both excitation conditions. We then proceeded to measure the relative scintillation intensity and decay kinetics of X-ray isoabsorbing diluted solutions of the $CsPbBr_3$ NC—so as to avoid inter-NC processes—under identical excitation and collection conditions. The integrated relative RL efficiencies are reported in Figure 3c, following a similar trend to Φ_X, thus highlighting the key role of the

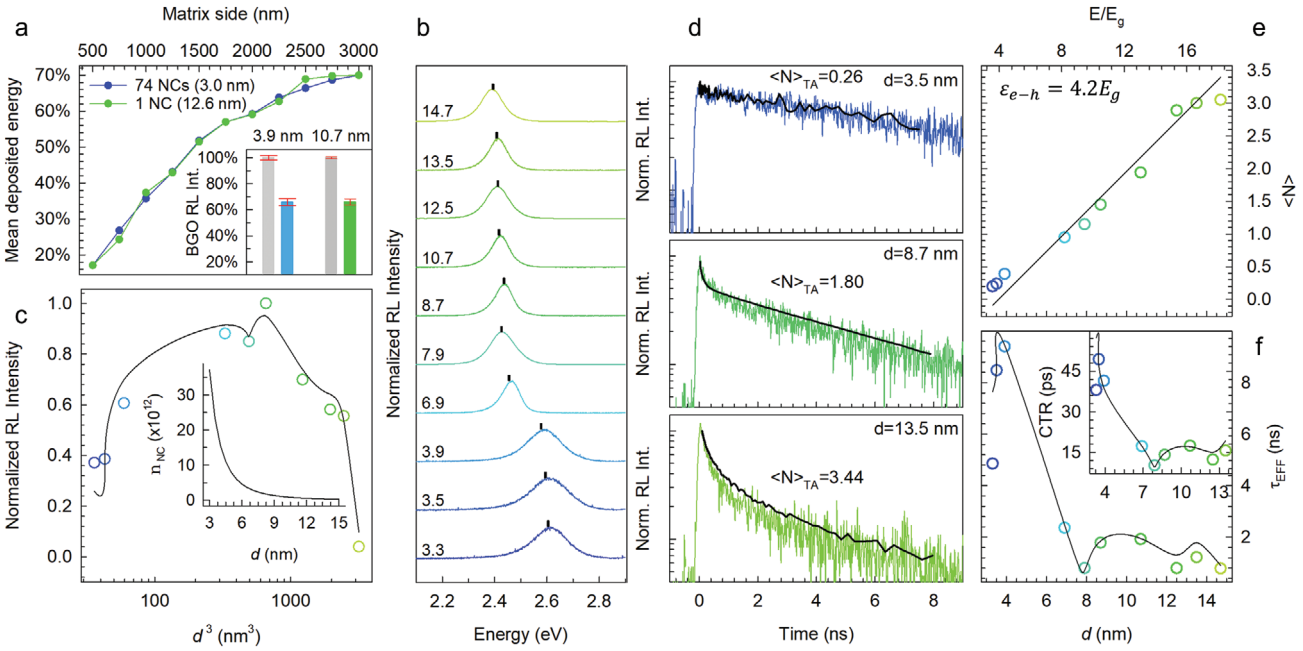

Figure 3. a) Geant4 simulation of the energy deposition in two samples containing the same mass of $CsPbBr_3$ in the form of one NC with d = 12.6 nm or 74 NCs with d = 3 nm (identical total volume of 2000 nm^3) of NCs. Inset: relative RL intensity of BGO in X-ray in the absence (grey) or in the presence of two solutions containing same mass of $CsPbBr_3$ NCs with d = 3.9 nm (blue bar) or d = 10.7 nm (green bar) corresponding in both cases to 34 ± 3% attenuation. b) RL spectra as a function of d (in nm as indicated). Thicks indicate the corresponding PL maximum. c) Relative RL intensity versus d^3. The solid line is the simulated trend according to Equation (7) multiplied by the number of NCs (n_{NC}). Inset: Number of NCs in 75 µL of octane solution (0.03 OD in 1 mm) versus NC size. d) Time resolved RL decay curves for the NCs with d = 3.5, 8.7, or 13.5 nm. The black lines are the TA kinetics at the corresponding ⟨*N*⟩. e) Experimental values of ⟨*N*⟩ with respect to the NC size and to the number of bandgaps predicted by Geant4 (top *x*-axis). The bottom axis is the particle size d as in "f." The black line is the best linear fit of the experimental data yielding the indicated electron-hole pair formation energy, $\varepsilon_{e\text{-}h}$ f. Effective lifetime extracted from the fit of time-resolved RL decays together with the simulated trend (solid line) obtained by solving Equations (5) and (6). Inset: estimated CTR values obtained setting τ_{RISE} = 100 *ps* and considering a LY = 10^4 ph MeV^{-1} for the d = 8.7 nm NC sample.

luminescence yield in the single exciton regime in the scintillation output. Time-resolved RL measurements complete the picture by providing direct evidence of the strong size dependence of ⟨*N*⟩ and of the *XX* decay rate and relative contribution under X-ray excitation. Specifically, Figure 3d shows the RL decay curves of three representative NC samples with *d* = 3.5, 8.7, and 13.5 nm (the complete set is shown in Figure S9, Supporting Information). The largest NCs showed multi-exponential kinetics with a fast *XX* component followed by the slower *X* decay.[26] In line with previous reports,[18,19] an intermediate component due to charged excitons was found ranging from 0.1 to 17% of the total signal. Most importantly, the relative weight of the *XX* contribution decreased gradually with decreasing *d*, resulting in the smallest particles showing only the *X* decay, which is consistent with the calculated small energy retention resulting in a negligible *XX* population. Following the typical approach for ultrafast kinetic studies in NCs, the ratio between the amplitudes of the *X* and *XX* components enables the estimation of ⟨*N*⟩ through Poissonian statistic.[33,36] Notably, as shown in Figure 3e, increasing the particle size resulted in the linear growth of ⟨*N*⟩, in remarkable agreement with the single particle energy-retention Monte Carlo simulations shown in the inset of Figure 1c and with the corresponding TA trace reported as black lines in Figure 3d, further confirming the correct quantification of the exciton occupancy. Expressing the emerging ⟨*N*⟩ as a function of the number of bandgap energies deposited within a single NC yielded an electron-hole pair formation energy of $\varepsilon_{e\text{-}h} = 4.2E_g$, which is slightly above the bulk limit in carrier multiplication processes as expected for quantum confined particles.[43] Also consistent with the TA data in Figure 2e, the *XX* decay component of the RL accelerated with decreasing particle size due to gradually stronger AR which also concomitantly led to a decrease of the respective relative weight. Overall, as shown in Figure 3f, this led to the acceleration of the experimental τ_{EFF}—extracted as the harmonic average of the *X*, *XX* and trion contributions—with increasing particle size despite the corresponding slower *XX* decay, thus further highlighting the relevance of the interaction with ionizing radiation over AR. It is important to note the opposite size dependence of the kinetics of scintillation, which accelerates with *d* due to its strongly biexcitonic nature, and that of PL, which instead slows down in large particles due to the increasing hybridization of the *s* and *p* states, which makes optical transitions symmetry forbidden.[46]

Using the experimental values for all scintillation parameters (i.e., ⟨*N*⟩, decay rates and efficiencies) without free parameters, we were able to use Equations (5)–(7) to model the evolution with the NC size of I_{SCINT}^{ENS} of same-mass ensembles of $CsPbBr_3$ NCs as well as their τ_{EFF}. To do so, we accounted for the different mass distributions across the sample set by scaling the single-particle I_{SCINT}^{NC} described by Equation (7) for the respective number of

NCs in the ensemble—estimated by dividing the total mass by the "molecular" weight of a single NC (inset of Figure 3c). We thereby obtained the scintillation intensity of NC ensembles expressed as, $I^{ENS}_{SCINT} = I^{NC}_{SCINT} \times n_{NC}$. The resulting simulated curve versus d is reported as a solid line in Figure 3c, showing an excellent match with the experimental values. Similarly, running Equations (5) and (6) with the experimentally measured lifetimes and $\langle N \rangle$-values describes the dependence of τ_{EFF} on the particle size (solid line in Figure 3f) thus further confirming the validity of the model. Finally, to provide a potentially technologically relevant insight into the timing performance of NCs, it is instructive to evaluate the impact of the NC size on the time resolution of more realistic NCs ensembles by calculating the *CTR* using literature *LY* for $CsPbBr_3$ NCs (e.g., $LY = 10^4$ ph MeV^{-1} for the $d = 8.7$ nm, corresponding to a light output of 5110 photons for 511 keV gamma excitation). By setting $\tau_{RISE} = 100\ ps$, we estimated the *CTR* shown in the inset of Figure 3f, which improves (decreases) gradually with increasing NC size and reaching potentially relevant values as fast as 15 ps or so, a trend again predicted by the simulations in Figure 1a.

3. Conclusion

In conclusion, based on the observed trends, the single particle energy retention appears to dominate the scintillation mechanism of NCs, as it determines the initial exciton occupancy and hence the response regime to ionizing radiation. In particular, although the total stopping power is size-independent for the same mass samples, the use of large NCs leads to the deposition of larger amounts of energy inside each particle, which consequently results in a higher *LY*; at the same time, large sizes reduce the AR efficiency, increasing the efficiency of the *XX* decay with beneficial effects on the timing performance. In fact, the generally high Φ_{AR} in $CsPbBr_3$ NCs leads to a scintillation process in which the *X* decay represents the major contribution, resulting in the *LY* being determined by the luminescence quantum yield, highlighting the crucial role of the surface chemistry for defect passivation and ensuring the preservation of the optical properties of NCs after embedding in host matrices. On the other hand, the *XX* component is the key to accelerating τ_{EFF} and achieving high temporal resolutions for ToF applications, so optimizing its yield, especially in larger particles, is paramount. More generally, the agreement found between the theoretical description and the experimental data is particularly relevant as it demonstrates the nontrivial possibility of predicting the main features of a NC scintillator from first principles–all the parameters in the equations are experimentally measured and the model, therefore, anticipates the actual behavior–thus providing an extremely powerful tool for directing research toward the optimization of key material parameters. Furthermore, the theory-experiment agreement validates the approximations of neglecting trionic contributions to scintillation and considering the totality of high-order excitons as biexcitons, further simplifying the prediction of actual performance. These results therefore fill a gap in the understanding of the scintillation process at the nanoscale and provide useful guidelines for specific particle engineering as the forthcoming generation of fast and efficient scintillators. Finally, we anticipate that the independence of the total stopping power from the particle size and number, but with the same total mass suggests that the differences in behavior between isolated NCs with different dimensions may be reduced in composite nano scintillators with a high density of NCs, where the electron shower released by one particle may act as a secondary excitation source of other NCs, giving rise to cascading scintillation phenomena. The study of this regime requires a specific treatment, which will be dealt with in a separate study.

Supporting Information

Supporting Information is available from the Wiley Online Library or from the author.

Acknowledgements

This work was funded by Horizon Europe EIC Pathfinder program through project 101098649 – UNICORN, by the PRIN program of the Italian Ministry of University and Research (IRONSIDE project), by the European Union—NextGenerationEU through the Italian Ministry of University and Research under PNRR—M4C2-I1.3 Project PE_00000019 "HEAL ITALIA", by European Union's Horizon 2020 Research and Innovation programme under Grant Agreement No 101004761 (AIDAINNOVA). This research is funded and supervised by the Italian Space Agency (Agenzia Spaziale Italiana, ASI) in the framework of the Research Day "Giornate della Ricerca Spaziale" initiative through the contract ASI N. 2023-4-U.0. L. M. acknowledges the European Research Council through the ERC Advanced Grant n. 101095974 (NEHA).

Open access publishing facilitated by Universita degli Studi di Milano-Bicocca, as part of the Wiley - CRUI-CARE agreement.

Conflict of Interest

The authors declare no conflict of interest.

Data Availability Statement

The data that support the findings of this study are available from the corresponding author upon reasonable request.

Keywords

colloidal nanocrystal quantum dots, lead halide perovskites, multi exciton dynamics, radiation detection, scintillation

Received: September 3, 2024
Revised: November 18, 2024
Published online:

[1] a) M. Ito, S. J. Hong, J. S. Lee, *Biomed. Eng. Lett.* **2011**, *1*, 70; b) P. Lecoq, *Nucl. Instrum. Methods Phys. Res., Sect. A* **2016**, *809*, 130.
[2] P. Lecoq, C. Morel, J. O. Prior, D. Visvikis, S. Gundacker, E. Auffray, P. Križan, R. M. Turtos, D. Thers, E. Charbon, J. Varela, C. de La Taille, A. Rivetti, D. Breton, J.-F. Pratte, J. Nuyts, S. Surti, S. Vandenberghe, P. Marsden, K. Parodi, J. M. Benlloch, M. Benoit, *Phys. Med. Biol.* **2020**, *65*, 21RM01.
[3] R. Hanke, T. Fuchs, N. Uhlmann, *Nucl. Instrum. Methods Phys. Res., Sect. A* **2008**, *591*, 14.

[4] N. Faderl, Fast Decay Solid-State Scintillators For High-Speed X-Ray Imaging, *11159*, SPIE, **2019**, https://doi.org/10.1117/12.2532017.
[5] C. Dujardin, E. Auffray, E. Bourret-Courchesne, P. Dorenbos, P. Lecoq, M. Nikl, A. N. Vasil'ev, A. Yoshikawa, R.-Y. Zhu, *IEEE Trans. Nucl. Sci.* **2018**, *65*, 1977.
[6] M. Antonello, M. Caccia, R. Santoro, R. Ferrari, G. Gaudio, G. Polesello, L. Pezzotti, V. Chmill, A. Karadzhinova-Ferrer, I. Vivarelli, *Int. J. Modern Phys. A* **2021**, *36*, 2142017.
[7] G. F. Knoll, *Radiation Detection and Measurement*, John Wiley & Sons, Hoboken NJ **2010**.
[8] F. Maddalena, L. Tjahjana, A. Xie, Arramel, S. Z., H. Wang, P. Coquet, W. Drozdowski, C. Dujardin, C. Dang, M. D. Birowosuto, *Crystals* **2019**, *9*, 88.
[9] J. Terry, W. T. David, *J. Med. Imaging* **2017**, *4*, 011013.
[10] M. Conti, *Eur. J. Nucl. Med. Mol. Imaging* **2011**, *38*, 1147.
[11] S. Gundacker, R. Martinez Turtos, N. Kratochwil, R. H. Pots, M. Paganoni, P. Lecoq, E. Auffray, *Phys. Med. Biol.* **2020**, *65*, 025001.
[12] E. Auffray, B. Frisch, F. Geraci, A. Ghezzi, S. Gundacker, H. Hillemanns, P. Jarron, T. Meyer, M. Paganoni, K. Pauwels, M. Pizzichemi, P. Lecoq, *IEEE Trans. Nucl. Sci.* **2013**, *60*, 3163.
[13] Y. Zhou, J. Chen, O. M. Bakr, O. F. Mohammed, *ACS Energy Letters 2021 6*, 739.
[14] a) Y. N. Kharzheev, *Phys. Part. Nucl.* **2019**, *50*, 42; b) S. V. Afanasiev, A. Y. Boyarintsev, M. V. Danilov, I. F. Emeliantchik, Y. V. Ershov, I. A. Golutvin, B. V. Grinyov, E. Ibragimova, L. G. Levchuk, A. V. Litomin, A. M. Makankin, A. I. Malakhov, P. V. Moisenz, I. Nuritdinov, V. F. Popov, V. Y. Rusinov, N. M. Shumeiko, V. A. Smirnov, P. V. Sorokin, E. I. Tarkovskii, A. Tashmetov, S. E. Vasiliev, B. Yuldashev, N. I. Zamiatin, P. N. Zhmurin, *Phys. Res. Sect. A* **2016**, *818*, 26.
[15] a) M. Gandini, I. Villa, M. Beretta, C. Gotti, M. Imran, F. Carulli, E. Fantuzzi, M. Sassi, M. Zaffalon, C. Brofferio, L. Manna, L. Beverina, A. Vedda, M. Fasoli, L. Gironi, S. Brovelli, *Nat. Nanotechnol.* **2020**, *15*, 462; b) R. M. Turtos, S. Gundacker, S. Omelkov, B. Mahler, A. H. Khan, J. Saaring, Z. Meng, A. Vasil'ev, C. Dujardin, M. Kirm, I. Moreels, E. Auffray, P. Lecoq, *npj 2D Mater. Appl.* **2019**, *3*, 37.
[16] R. M. Turtos, S. Gundacker, A. Polovitsyn, S. Christodoulou, M. Salomoni, E. Auffray, I. Moreels, P. Lecoq, J. Q. Grim, *J. Instrum.* **2016**, *11*, P10015.
[17] a) T. J. Hajagos, C. Liu, N. J. Cherepy, Q. Pei, *Adv. Mater.* **2018**, *30*, 1706956; b) P. Qibing, Proc. SPIE, **2023**, https://doi.org/10.1117/12.2679205.
[18] A. Erroi, S. Mecca, M. L. Zaffalon, I. Frank, F. Carulli, A. Cemmi, I. Di Sarcina, D. Debellis, F. Rossi, F. Cova, K. Pauwels, M. Mauri, J. Perego, V. Pinchetti, A. Comotti, F. Meinardi, A. Vedda, E. Auffray, L. Beverina, S. Brovelli, *ACS Energy Lett.* **2023**, *8*, 3883.
[19] A. Erroi, F. Carulli, F. Cova, I. Frank, M. L. Zaffalon, J. Llusar, S. Mecca, A. Cemmi, I. Di Sarcina, F. Rossi, L. Beverina, F. Meinardi, I. Infante, E. Auffray, S. Brovelli, *ACS Energy Lett.* **2024**, *9*, 2333.
[20] a) L. A. Padilha, W. K. Bae, V. I. Klimov, J. M. Pietryga, R. D. Schaller, *Nano Lett.* **2013**, *13*, 925; b) Z. Meng, B. Mahler, J. Houel, F. Kulzer, G. Ledoux, A. Vasil'ev, C. Dujardin, *Nanoscale* **2021**, *13*, 19578; c) Z. Meng, B. Mahler, J. Houel, F. Kulzer, A. Vasil'ev, C. Dujardin, *Mater. Adv.* **2022**, *3*, 8341.
[21] J. H. Heo, D. H. Shin, J. K. Park, D. H. Kim, S. J. Lee, S. H. Im, *Adv. Mater.* **2018**, *30*, 1801743.
[22] a) O. D. I. Moseley, T. A. S. Doherty, R. Parmee, M. Anaya, S. D. Stranks, *J. Mater. Chem. C* **2021**, *9*, 11588; b) R. Gu, K. Han, J. Jin, H. Zhang, Z. Xia, *Chem. Mater.* **2024**, *36*, 2963; c) A. Wibowo, M. A. K. Sheikh, L. J. Diguna, M. B. Ananda, M. A. Marsudi, A. Arramel, S. Zeng, L. J. Wong, M. D. Birowosuto, *Commun. Mater.* **2023**, *4*, 21; d) Z. Xu, X. Tang, Y. Liu, Z. Zhang, W. Chen, K. Liu, Z. Yuan, *ACS Appl. Mater. Interfaces* **2019**, *11*, 14191; e) K. Děcká, A. Suchá, J. Král, I. Jakubec, M. Nikl, V. Jarý, V. Babin, E. Mihóková, V. Čuba, *Nanomaterials* **2021**, *11*, 1935. f) F. Liu, R. Wu, Y. Zeng, J. Wei, H. Li, L. Manna, A. D. Mohite, *Nanoscale* **2022**, *14*, 6743; g) I. H. B. Braddock, M. Al Sid Cheikh, J. Ghosh, R. E. Mulholland, J. G. O'Neill, V. Stolojan, C. Crean, S. J. Sweeney, P. J. Sellin, *Nanomaterials* **2022**, *12*, 2141.
[23] M. L. Zaffalon, F. Cova, M. Liu, A. Cemmi, I. Di Sarcina, F. Rossi, F. Carulli, A. Erroi, C. Rodà, J. Perego, A. Comotti, M. Fasoli, F. Meinardi, L. Li, A. Vedda, S. Brovelli, *Nat. Photonics* **2022**, *16*, 860.
[24] Q. Chen, J. Wu, X. Ou, B. Huang, J. Almutlaq, A. A. Zhumekenov, X. Guan, S. Han, L. Liang, Z. Yi, J. Li, X. Xie, Y. Wang, Y. Li, D. Fan, D. B. L. Teh, A. H. All, O. F. Mohammed, O. M. Bakr, T. Wu, M. Bettinelli, H. Yang, W. Huang, X. Liu, *Nature* **2018**, *561*, 88.
[25] W. Chen, Y. Liu, Z. Yuan, Z. Xu, Z. Zhang, K. Liu, Z. Jin, X. Tang, *J. Radioanal. Nucl. Chem.* **2017**, *314*, 2327.
[26] A. Anand, M. L. Zaffalon, A. Erroi, F. Cova, F. Carulli, S. Brovelli, *A. C. S. Energy Lett.* **2024**, *9*, 1261.
[27] M. C. De Siena, V. V. Klepov, S. P. Stepanoff, K. S. Bayikadi, L. Pan, I. R. Pandey, S. Karki, D. Y. Chung, D. E. Wolfe, M. G. Kanatzidis, *Adv. Mater.* **2023**, *35*, 2303244.
[28] S. Mecca, F. Pallini, V. Pinchetti, A. Erroi, A. Fappani, F. Rossi, S. Mattiello, G. M. Vanacore, S. Brovelli, L. Beverina, *ACS Appl. Nano Mater.* **2023**, *6*, 9436.
[29] F. Cova, A. Erroi, M. L. Zaffalon, A. Cemmi, I. Di Sarcina, J. Perego, A. Monguzzi, A. Comotti, F. Rossi, F. Carulli, S. Brovelli, *Nano Lett.* **2024**, *24*, 905.
[30] a) K. Děcká, F. Pagano, I. Frank, N. Kratochwil, E. Mihóková, E. Auffray, V. Čuba, *J. Mater. Chem. C* **2022**, *10*, 12836; b) F. Pagano, J. Král, K. Děcká, M. Pizzichemi, E. Mihóková, V. Čuba, E. Auffray, *Adv. Mater. Interfaces* **2024**, *11*, 2300659; c) A. Erroi, S. Mecca, M. L. Zaffalon, I. Frank, F. Carulli, A. Cemmi, I. Di Sarcina, D. Debellis, F. Rossi, F. Cova, *ACS Energy Lett.* **2023**, *8*, 3883.
[31] a) A. Forde, D. Kilin, *J. Chem. Theory Comput.* **2021**, *17*, 7224; b) L. Gao, Q. Li, J.-L. Sun, Q. Yan, *J. Phys. Chem. Lett.* **2023**, *14*, 1165; c) H. Huang, M. I. Bodnarchuk, S. V. Kershaw, M. V. Kovalenko, A. L. Rogach, *ACS Energy Lett.* **2017**, *2*, 2071.
[32] a) F. Pagano, N. Kratochwil, M. Salomoni, M. Pizzichemi, M. Paganoni, E. Auffray, *Phys. Med. Biol.* **2022**, *67*, 135010; b) Y. Zhang, R. Sun, X. Ou, K. Fu, Q. Chen, Y. Ding, L.-J. Xu, L. Liu, Y. Han, A. V. Malko, X. Liu, H. Yang, O. M. Bakr, H. Liu, O. F. Mohammed, *ACS Nano* **2019**, *13*, 2520; c) L. Wang, K. Fu, R. Sun, H. Lian, X. Hu, Y. Zhang, *Nano-Micro Lett.* **2019**, *11*, 52.
[33] V. I. Klimov, *J. Phys. Chem. B* **2000**, *104*, 6112.
[34] a) I. Robel, R. Gresback, U. Kortshagen, R. D. Schaller, V. I. Klimov, *Phys. Rev. Lett.* **2009**, *102*, 177404; b) R. Vaxenburg, A. Rodina, A. Shabaev, E. Lifshitz, A. L. Efros, *Nano Lett.* **2015**, *15*, 2092.
[35] a) S. Agostinelli, J. Allison, K. Amako, J. Apostolakis, H. Araujo, P. Arce, M. Asai, D. Axen, S. Banerjee, G. Barrand, F. Behner, L. Bellagamba, J. Boudreau, L. Broglia, A. Brunengo, H. Burkhardt, S. Chauvie, J. Chuma, R. Chytracek, G. Cooperman, G. Cosmo, P. Degtyarenko, A. Dell'Acqua, G. Depaola, D. Dietrich, R. Enami, A. Feliciello, C. Ferguson, H. Fesefeldt, G. Folger, et al., *Nucl. Instrum. Methods Phys. Res., Sect. A* **2003**, *506*, 250.
[36] N. S. Makarov, S. Guo, O. Isaienko, W. Liu, I. Robel, V. I. Klimov, *Nano Lett.* **2016**, *16*, 2349.
[37] Y. Li, T. Ding, X. Luo, Z. Chen, X. Liu, X. Lu, K. Wu, *Nano Res.* **2019**, *12*, 619.
[38] J. Aneesh, A. Swarnkar, V. Kumar Ravi, R. Sharma, A. Nag, K. V. Adarsh, *J. Phys. Chem. C* **2017**, *121*, 4734.
[39] a) K. Děcká, J. Král, F. Hájek, P. Průša, V. Babin, E. Mihóková, V. Čuba, *Nanomaterials* **2022**, *12*, 14. b) T. Skrypnyk, O. Viahin, I. Bespalova, O. Zelenskaya, V. Tarasov, V. Alekseev, S. Yefimova, O. Sorokin, *Radiat. Meas.* **2023**, *169*, 107028.
[40] C. Livache, W. D. Kim, H. Jin, O. V. Kozlov, I. Fedin, V. I. Klimov, *Nat. Photonics* **2022**, *16*, 433.

[41] C. Galland, Y. Ghosh, A. Steinbrück, M. Sykora, J. A. Hollingsworth, V. I. Klimov, H. Htoon, *Nature* **2011**, *479*, 203.
[42] R. C. Alig, S. Bloom, *Phys. Rev. Lett.* **1975**, *35*, 1522.
[43] a) L. A. Padilha, J. T. Stewart, R. L. Sandberg, W. K. Bae, W.-K. Koh, J. M. Pietryga, V. I. Klimov, *Acc. Chem. Res.* **2013**, *46*, 1261; b) J. T. Stewart, L. A. Padilha, W. K. Bae, W.-K. Koh, J. M. Pietryga, V. I. Klimov, *J. Phys. Chem. Lett.* **2013**, *4*, 2061.
[44] a) A. Shabaev, A. L. Efros, A. J. Nozik, *Nano Lett.* **2006**, *6*, 2856; b) V. I. Klimov, *J. Phys. Chem. B* **2006**, *110*, 16827.
[45] a) M. C. Brennan, J. E. Herr, T. S. Nguyen-Beck, J. Zinna, S. Draguta, S. Rouvimov, J. Parkhill, M. Kuno, *J. Am. Chem. Soc.* **2017**, *139*, 12201; b) V. I. Klimov, *Nanocrystal Quantum Dots*, CRC Press, Boca Raton, FL **2017**.
[46] F. Krieg, P. C. Sercel, M. Burian, H. Andrusiv, M. I. Bodnarchuk, T. Stöferle, R. F. Mahrt, D. Naumenko, H. Amenitsch, G. Rainò, M. V. Kovalenko, *ACS Cent. Sci.* **2021**, *7*, 135.
[47] V. I. Klimov, *Ann. Rev. Phys. Chem.* **2007**, *58*, 635.
[48] a) M. N. Ashner, K. E. Shulenberger, F. Krieg, E. R. Powers, M. V. Kovalenko, M. G. Bawendi, W. A. Tisdale, *ACS Energy Lett.* **2019**, *4*, 2639; b) J. A. Castañeda, G. Nagamine, E. Yassitepe, L. G. Bonato, O. Voznyy, S. Hoogland, A. F. Nogueira, E. H. Sargent, C. H. B. Cruz, L. A. Padilha, *ACS Nano* **2016**, *10*, 8603.